Instability, Evolution, and Mixing in Stratified Shear Flow as a Function of Richardson Number

Joseph Werne[(1)] and B.A. Pettersson-Reif[(2)]

[(1)]NorthWest Research Associates, Boulder, CO, USA
werne@cora.nwra.com
[(2)]Forsvarets Forskningsinstitutt (FFI), Kjeller, Norway
bjorn.reif@ffi.no

Abstract

High-resolution direct-numerical simulations of the Kelvin-Helmholtz instability reveal flow morphologies and evolutions that depend strongly on the Richardson number Ri. The highest $Ri = 0.2$ case studied displays flat KH billows that become turbulent immediately upon billow formation, with turbulence appearing in the cores and then migrating laterally as time progresses. In contrast, the lowest $Ri = 0.05$ case exhibits coherent KH billows with round cross sections and rapid solid-body rotation that stabilizes them and delays the onset of turbulence in the billow cores. This results in a complex sequence of transitions at low Ri that include 1) layered billow formation, 2) secondary instability of billow edges, 3) vigorous turbulence in the braid region between billow cores, and 4) later development of turbulence in the cores. Despite these stark differences, the final flow states exhibit nearly identical mid-layer stability profiles and shear/buoyancy timescale ratios N/S for all Ri, providing useful guidance for layer parameterization.

1 Introduction

Stratified shear turbulence influences the transport of momentum, heat, kinetic energy, and particulate matter for a host of important problems, such as the near-surface atmospheric and oceanic boundary layers, coupling across the tropopause and above in earth's atmosphere, and the near-surface and sub-tachocline shear layers in the solar interior. To study the dynamics, evolution, and mixing in such layers, we employ high-resolution direct-numerical simulations (DNS) of the Kelvin-Helmholtz instability for a range of stratifications quantified by the Richardson number Ri. In order to examine equally vigorous turbulent motions for all Ri studied here, we increase the Reynolds number Re with Ri so that similar length-scale ranges result for all simulations conducted.

All simulations are carried out using the NWRA Triple code, which is a pseudo-spectral Boussinesq solver employing the third-order Runge-Kutta time-stepping algorithm of Spalart et al. (1991) to advance the coefficients for a spectral representation of laterally periodic Fourier modes and either sine or cosine series in the vertical, depending on the parity of the field variable being represented. An efficient 3D fast-Fourier transform algorithm is used to move between spectral and physical space (Werne et al., 2005).

2 Problem Formulation

Hyperbolic-tangent velocity $U = U_0 \tanh(z/h)$ and linear temperature $T = \beta z$ profiles are used to initiate shear flow in a $4\lambda \times 2\lambda \times 2\lambda$ Cartesian geometry, where λ is the wavelength of the most unstable asymptotic linear mode. Here U_0, h, and β are the velocity amplitude, initial half-shear-layer depth, and mean background temperature gradient, respectively,

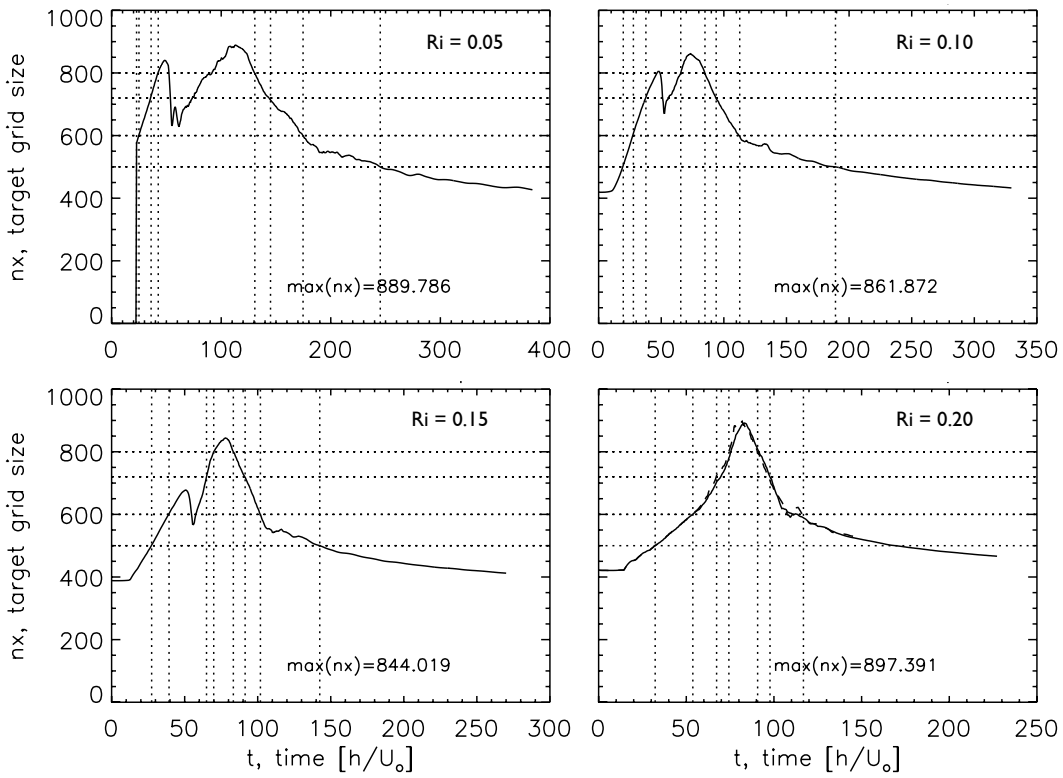

Figure 1: Time-evolving resolution requirements per wavelength λ for Ri=0.05, Re=2500 (upper left), Ri=0.10, Re=2800 (upper right), Ri=0.15, Re=2900 (lower left), and Ri=0.20, Re=4000 (lower right).

and z denotes the vertical dimension. Top and bottom domain boundaries have fixed temperature and are impenetrable and stress free.

Initial values of the midlayer Richardson number are given by $Ri = 0.05$, 0.1, 0.15, and 0.2, and corresponding values of the Reynolds numbers we use are $Re = 2500$, 2800, 2900, and 4000, respectively, where $Ri = g\alpha\beta h^2/U_0^2$ and $Re = U_0 h/\nu$. For all simulations, the Prandtl number is held fixed at $Pr = \nu/\kappa = 1$. Here g, α, ν, and κ are the acceleration due to gravity, thermal-expansion, kinematic-viscosity, and thermal-diffusion coefficients, respectively.

3 Resolution Requirements

Figure 1 shows the time evolution of the maximum number of spectral modes $max(nx) = \lambda/(1.8\eta)$ needed per wavelength λ for all simulations conducted. Here $\eta = (\nu^3/\epsilon)^{1/4}$ is the Kolmogorov length scale and ϵ is the average rate of kinetic energy dissipation.

While the detailed evolution of the required number of spectral modes differs for different Ri, maximum values all peak at roughly $max(nx) = 900$, indicating the values we chose for Re result in the same range of spectral modes, as was our intent. The $4\lambda \times 2\lambda \times 2\lambda$ domains we simulate require up to $3600 \times 1800 \times 1800$ spectral modes for all of the cases presented here.

For $Ri \leq 0.15$, the resolution requirements revealed in Figure 1 exhibit a double-peaked structure, while at $Ri = 0.2$ a single-peak structure exists. This is because turbulence erupts initially in the periphery of the KH billows for low Ri, and then it erupts again later in the billow cores, while at high Ri turbulence peaks only in the billow cores and

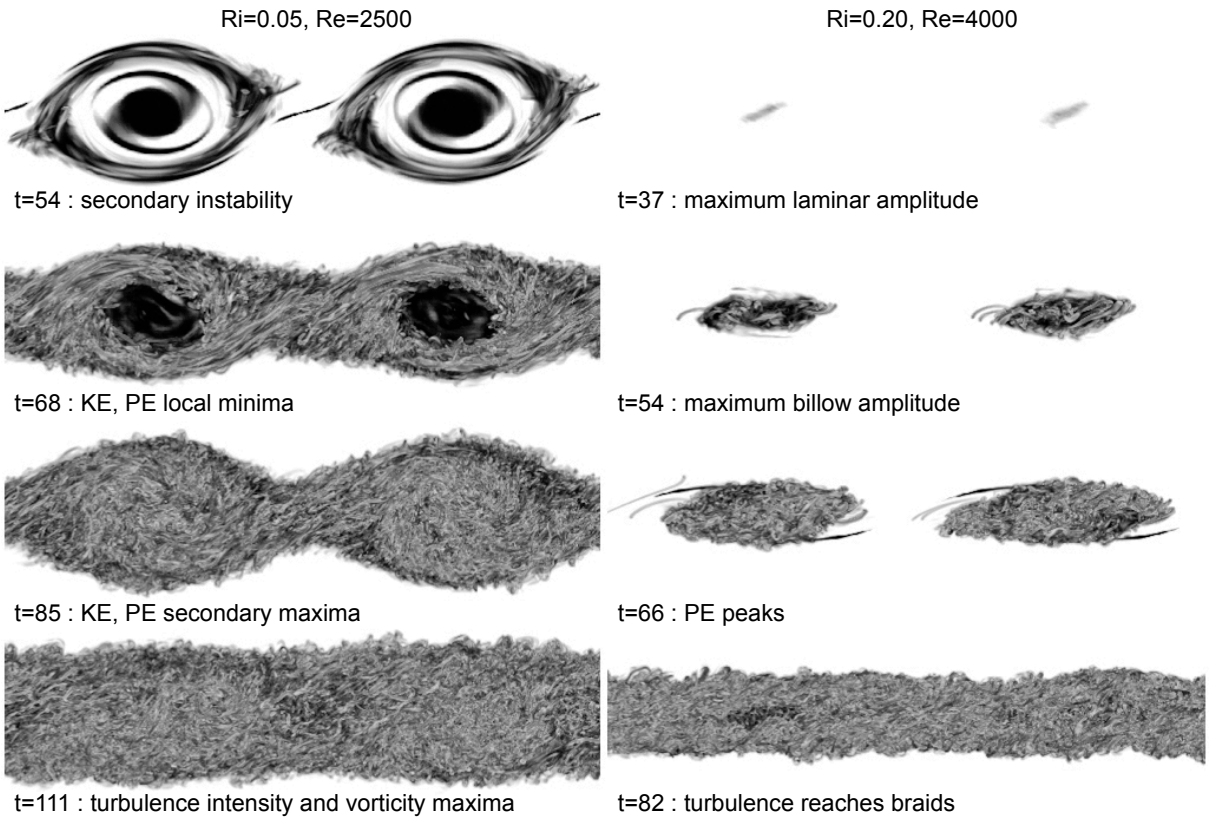

Figure 2: KH layer morphology viewed from the side for two billows for $Ri = 0.05$ (left panel) and $Ri = 0.2$ (right panel) at four distinct times during the flow evolution. Visualization is achieved by depicting $\lambda_2 < 0$, which reveals the vortex tubes in the flow. See text for discussion.

then gradually migrates out from there.

4 Flow Morphology

Figure 2 shows the evolving morphology of the flow with time by depicting the vortex tubes in the flow for the lowest (left) and highest (right) Ri values studied. Vortex tubes are indicated by negative values of λ_2, which is the intermediate eignenvalue of $S^2 + R^2$, where S and R are the strain and rotation matrices, respectively (Jeong and Hussain, 1995). The initial development of turbulence in the periphery of a KH billow for $Ri = 0.05$ is well established, e.g., see Peltier and Caulfield (2003). It results there because the stable overturning of a primary KH billow produces alternating layers of stable and unstable fluid stratification at the billow periphery, and eventually the unstable layers overturn, producing a secondary instability aligned orthogonally to the primary billow. As a result turbulence appears first in the billow periphery, and then later it erupts in the billow core when vortical motion finally invades that region. As is evident in Figure 1, the appearance of turbulence in the billow cores is more vigorous and achieves smaller dissipation length scales than the initial appearance in the billow periphery, and this dominance by the billow-core turbulence becomes more pronounced as Ri is increased and the separate turbulence-eruption events merge and become one at $Ri = 0.20$. In this latter case, turbulence appears immediately upon overturning of the billow, as the core region is itself convectively unstable, and the primary billow overturns so weakly that the

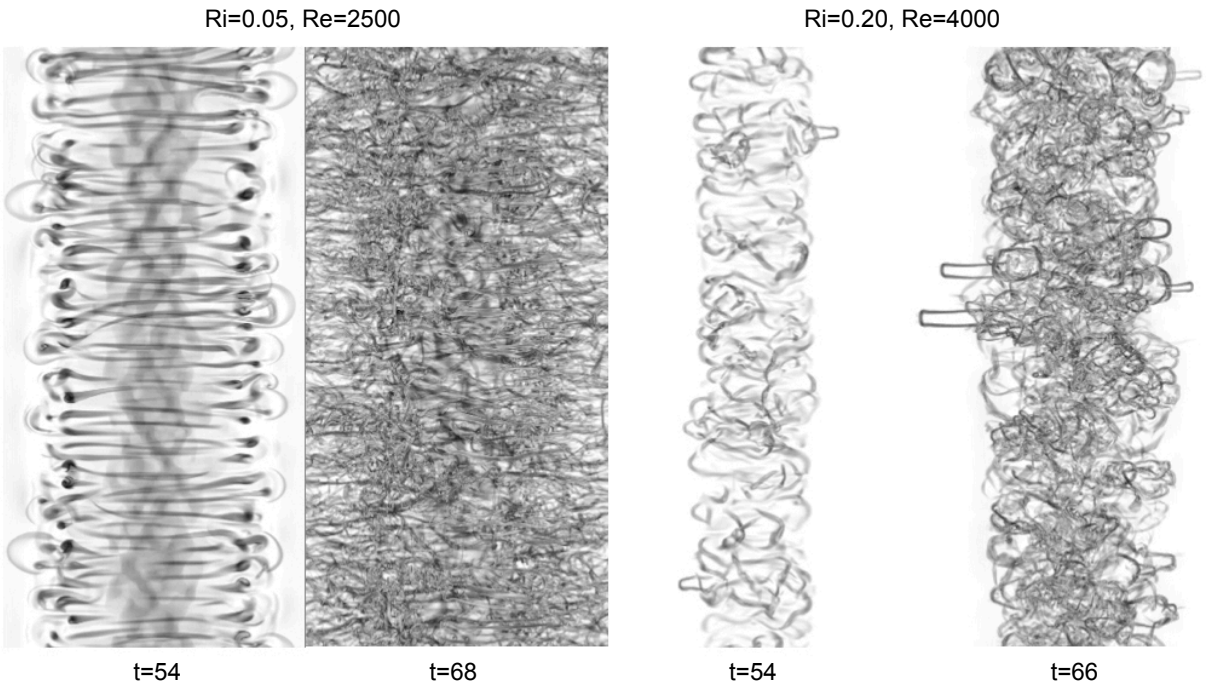

Figure 3: KH layer morphology viewed from above for a single billow for $Ri = 0.05$ (left panel) and $Ri = 0.2$ (right panel) at two distinct times during the flow evolution. Visualization is achieved by depicting $\lambda_2 < 0$, which reveals the vortex tubes in the flow. See text for discussion.

stabilizing influence of rotation is insufficient to maintain core stability.

A consequence of the immediate development of turbulence in the billow cores for $Ri = 0.2$ is that the stable braid regions between neighboring billows are maintained, effectively keeping the billows separated well into the evolution of the flow. In fact the braids are so stable for $Ri = 0.2$ that they are only penetrated by vortical motion when self-propagating vortex loops in the form of long-legged hairpins spontaneously form in the billow cores. These hairpins can be seen at $t = 66$ in the right side of Figure 2.

Figure 3 shows the view from above for a single billow at $t = 54$ and $t \approx 67$ for $Ri = 0.05$ (left) and $Ri = 0.2$ (right). Figure 3 clearly shows the stability of the billow cores resulting from their near-solid-body rotation for $Ri = 0.05$ by visualizing waves there at $t = 54$; it also shows the view from above of the self-propagating hairpin loops moving from the core region for $Ri = 0.2$ at $t = 66$.

Figure 4 depicts the smooth transition in morphology from the rotation-stabilized KH billows at $Ri = 0.05$ and $Ri = 0.1$ and the convectively unstable billow cores at $Ri = 0.15$ and $Ri = 0.2$. Figure 4 clearly shows turbulence first in the braid regions between neighboring billows while the billow cores maintain their stability for the lower two Ri values. It also shows the core turbulence and maintained braid stability for the higher two Ri values. This dichotomy indicates a fundamental shift in the evolution and dynamics between $Ri = 0.1$ and $Ri = 0.15$ when comparable levels of small-scale turbulent motion exist as Ri is varied.

5 Final Layer Properties

Despite the fundamentally different evolutions for the high- and low-Ri shear layers demonstrated in Figures 1-4, in this section we show that important aspects of the late-

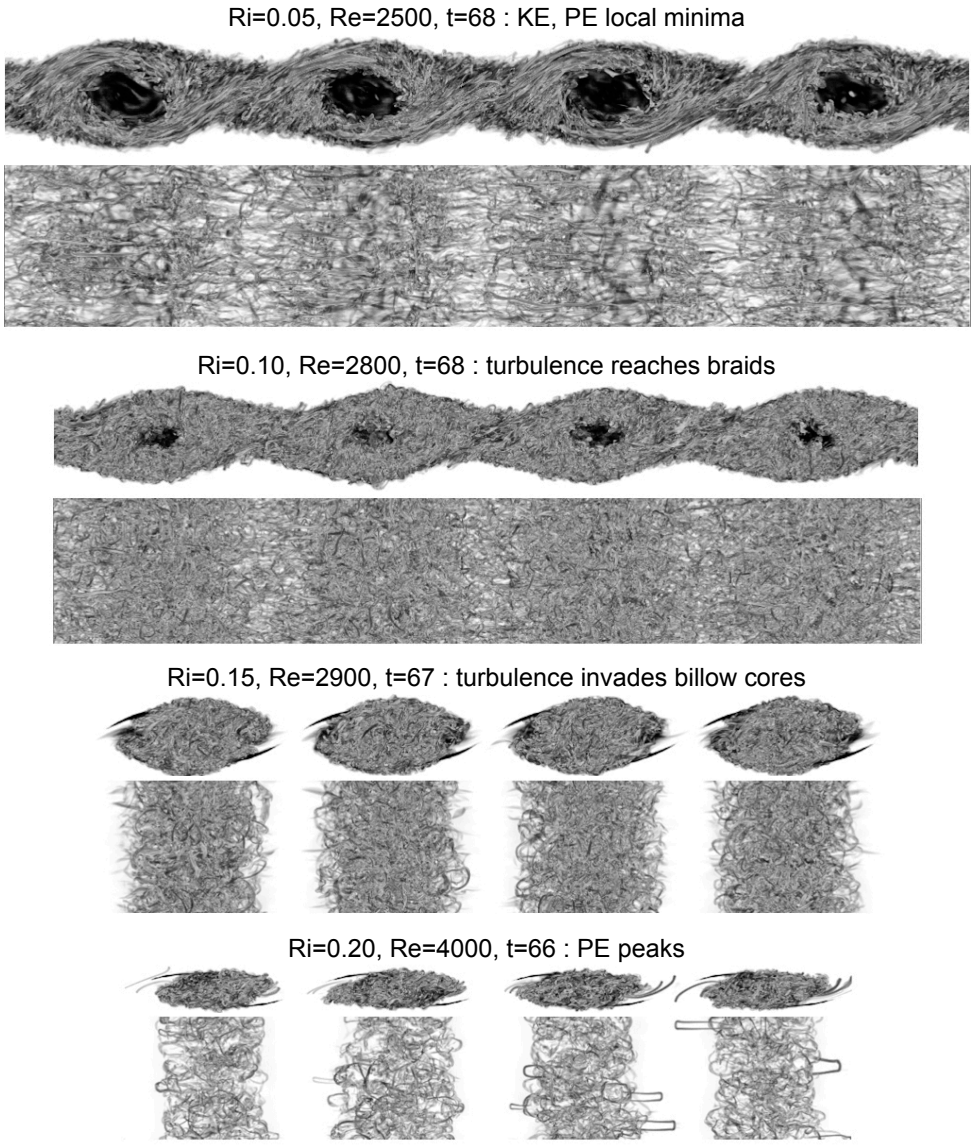

Figure 4: KH layer morphology for four different *Ri-Re* pairs viewed from the side and from above. Visualization is achieved by depicting $\lambda_2 < 0$, which reveals the vortex tubes in the flow. See text for discussion.

time layer can be reasonably estimated using simple conservation-of-energy arguments. First, we note that once complete, vertical and lateral mixing inside the turbulent shear layer will produce a final layer depth L that scales as $L/h \approx Ri^{-1/2}$. Second, we estimate that the final-layer bulk Richardson number Ri_L assumes a constant value. And third, we show that refinement of this estimate allowing for imperfect lateral mixing before motion and further evolution ceases gives $N/S \approx 1$, where N is the background Brunt-Vaisala frequency and S is the magnitude of the total mean shear rate $2S_{ij} = \partial_i U_j + \partial_j U_i$.

We begin by noting that in the limit of large final layer depth L, the initial kinetic energy per unit volume of the mean flow is $KE_1 \approx U_0^2$. Also, the initial potential energy per unit volume is $PE_1 \approx 2/3\alpha\beta g L^2$, where $z = L$ is the final height to which we integrate the kinetic energy. Likewise, for complete vertical and lateral mixing inside the fully evolved shear layer, the final kinetic energy is $KE_2 \approx U_0^2/3$, and the final potential energy inside the layer is $PE_2 \approx 0$. Equating initial and final total energy

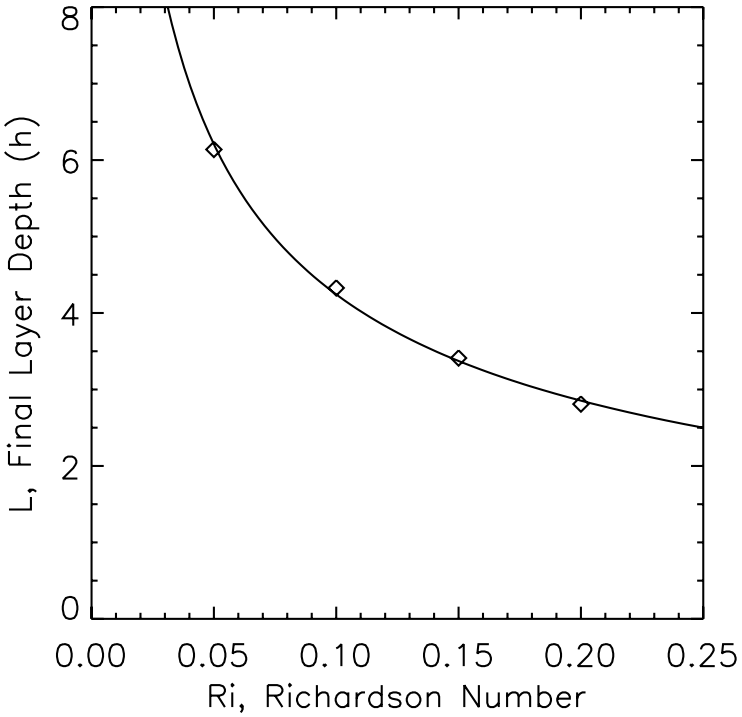

Figure 5: Final shear-layer depth L versus Richardson number Ri.

$KE_1 + PE_1 \approx KE_2 + PE_2$, we have $L/h \approx Ri^{-1/2}$ and $Ri_L \approx 1$.

Figure 5 shows the measured final layer depth for the four values of Ri we examined. The curve included in the graph is given by $L/h = 1.5Ri^{-1/2} - 0.5$, demonstrating the anticipated form, with a correction for finite L/h.

Figure 6 shows the measured bulk Richardson number Ri_L versus time (left panel) based on the layer depth L. It shows late-time convergence of Ri_L for the largest and smallest Ri values studied. A curiosity of the graph, however, is the unexpected spike in Ri_L for the $Ri = 0.2$ case. This results from incomplete lateral mixing of the layer at intermediate times when the vertical derivative of the mean velocity alone does not account for a sufficient fraction of the mean shear rate S. We can account for this by examining the measured bulk value of N/S versus time, which is included in the right panel of the figure. Here we see that the anomalous spike in Ri_L for $Ri = 0.2$ does not occur for N/S.

6 Conclusions

We have demonstrated that the transition to turbulence and basic flow morphology depend sensitively on Ri for stratified shear flow when the Reynolds number is adjusted so that all cases studied achieve the same range of dynamical length scales. A fundamental change in the evolution of the flow appears above and below a critical Richardson number between $Ri = 0.1$ and $Ri = 0.15$. Whereas the lower-Ri cases exhibit stabilization of the primary KH billows due to their near-solid-body rotation, leading to a delayed transition to turbulence in the billow cores that gives rise to secondary instability first in the billow peripheries, the billow cores for the higher-Ri cases immediately transition to turbulent

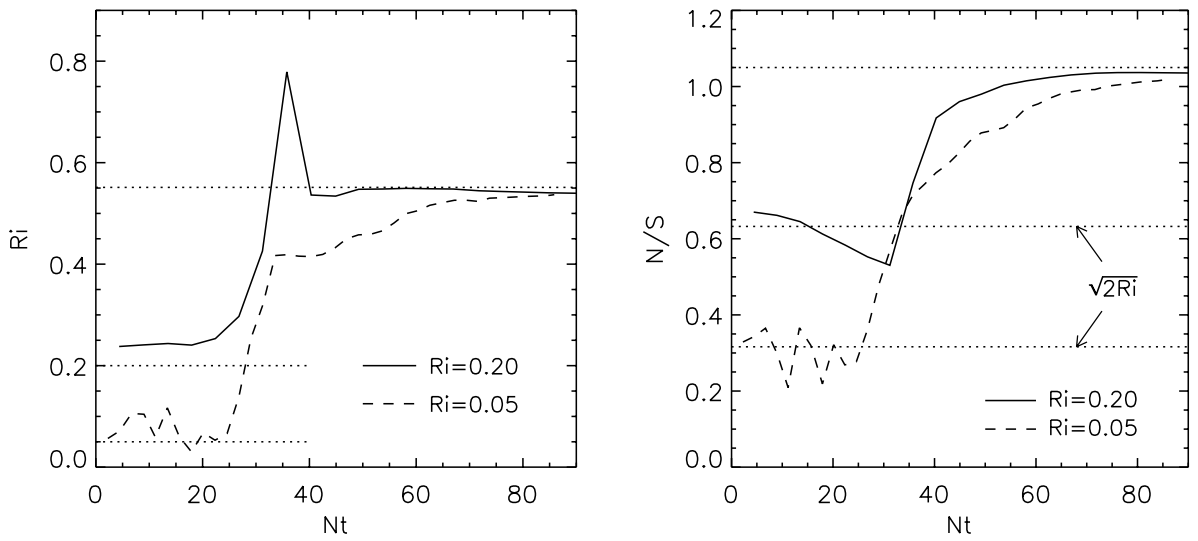

Figure 6: Layer bulk Richardson number (left panel) and timescale ratio N/S (right panel) for $Ri = 0.2$ (solid line) and $Ri = 0.05$ (dashed line) versus Nt. N, S, and t are the buoyancy frequency, mean shear rate, and time, respectively.

motion upon overturning just once. Despite these different pathways through instability and turbulence, however, both high- and low-Ri cases exhibit final states whose bulk characteristics can be reasonably understood via very simple conservation-of-energy arguments, leading to final layer depths that scale as $L/h \sim Ri^{-1/2}$ and final bulk Richardson numbers Ri_L that converge to a constant value.

References

Jeong, J. and Hussain, F. (1995). On the Identification of a Vortex. *J. Fluid Mech.*, 285:69–94.

Peltier, W. and Caulfield, C. (2003). Mixing Efficiency in Stratified Shear Flows. *Annu. Rev. Fluid Mech.*, 35:135–167.

Spalart, P., Moser, R., and Rogers, M. (1991). Spectral methods for the Navier-Stokes equations with one infinite and two periodic directions. *J. Comput. Phys.*, 96:297–324.

Werne, J., Lund, T., Pettersson-Reif, B., Sullivan, P., and Fritts, D. (2005). CAP Phase II Simulations for the Air Force HEL-JTO Project: Atmospheric Turbulence Simulations on NAVO's 3000-Processor IBM P4+ and ARL's 2000-Processor Intel Xeon EM64T Cluster. *15th DoD HPC User Group Conference, June, Nashville, TN*, page DOI:10.1109/DODUGC.2005.16.